Supporting Information for:

Emergence of chromatin hierarchical loops from protein disorder and nucleosome asymmetry.

Akshay Sridhar[1], Stephen E. Farr[1], Guillem Portella[2], Tamar Schlick[3,4,5], Modesto Orozco[6,7], Rosana Collepardo-Guevara[1,2,8*]

[1]Maxwell Centre, Cavendish Laboratory, University of Cambridge, JJ Thomson Avenue, CB3 0HE Cambridge, UK. [2]Chemistry Department, University of Cambridge, Lensfield Road, Cambridge, CB2 1EW, UK. [3]Department of Chemistry, New York University, 100 Washington Square East, New York, NY 10003, USA. [4]Courant Institute of Mathematical Sciences, New York University, 251 Mercer Street, New York, NY 10012, USA. [5]New York University-East China Normal University Center for Computational Chemistry, New York University, 3663 North Zhongshan Road, Shanghai, 200062, China [6]Institute for Research in Biomedicine, The Barcelona Institute of Science and Technology, Baldiri i Reixac 19. 08028, Barcelona, Spain. [7]Department of Biochemistry and Biomedicine. University of Barcelona. Av. Diagonal 647. 08028, Barcelona, Spain. [8]Department of Genetics, University of Cambridge, Cambridge, CB2 3EH, UK.

Corresponding Author: * rc597@cam.ac.uk

www.pnas.org/cgi/doi/10.1073/pnas.1910044117

Supporting Discussion

Structure of the NTD and GD of the nucleosome bound H1

Because of its short length, the NTD plays a negligible role in shielding entering/exiting linker DNA electrostatic repulsion (1). Instead, the NTD has been postulated to act as an 'anchor' that secures the linker histone to the nucleosome and counterbalances the fluctuating interactions between the CTD and the DNA linkers (2). In SI Figure 2, we show that the NTD adopts a significant helical population upon DNA binding. Interestingly, this disordered-to-ordered transition of the NTD is dependent on DNA interaction as the isolated NTD remains disordered in solution.

It has been observed that the GD of H1 adopts a stable winged-helix fold (3) and its nucleosome binding location varies across isoforms and with the experimental conditions (4–6). For instance, while chicken H5 (7) and Xenopous laevis histone H1.0 (8) bind in a symmetric on-dyad mode, Drosophila H1 (9) and human H1.4 (10) exhibit asymmetric off-dyad binding modes. Cryo-EM of a 12-nucleosome array (10) suggested variability in the localization of the H1 globular head across the array. Recent mesoscale modelling of chromatin arrays comparing different H1 densities and subtypes that bind on-dyad or off-dyad revealed that some variations produce highly compact, but rigid chromatin fibers, while others decrease compaction, but enhance long-range interactions promoting looping (11). In agreement with the experimental data our model is based on (8), we observe that the H1.0 GD remains bound 'on-dyad' to the nucleosomal DNA, preserves its winged-helix fold throughout the simulations (Figure S3A), and is rigid when compared to the CTD (Figure 2B). We also see that GD's binding to the nucleosome is mainly stabilized by electrostatic contacts (Figure S3B), which are consistent with isothermal titration calorimetry (ITC) experiments (7).

Partitioning of the disordered CTD of the nucleosome bound H1 into four different loops

The statistical ensembles of the CTD of the nucleosome bound H1, obtained with BEMetaD (see below), reveal that, independently of the force field (Figure S1), this domain can be divided into four different regions. We term these four regions: 'beta', 'loop 1', 'loop 2' and 'end' (Figure 2D) based on their structural charactheristics. Each region spatially concentrates ~8-10 positively charged residues (lysines/arginines) and exhibits distinct patterns of interactions with the DNA in the nucleosome (see Figure 2D). Together, they efficiently screen the repulsion among exiting/entering DNA linkers but each confers different levels of flexibility to the DNA linkers. Interestingly, the CTD regions that are least flexible (beta and loop 2) are found sandwiched between the two DNA linkers right at their crossing point. These two regions interact strongly (Figure 2D) with both DNA linkers around the crossing point, contributing to narrowing the distance within the nucleosome particle (Figure 3A).

The 'beta' region involves the only stable secondary element present in the CTD (occurring in ~80% of the frames analysed). This is a 22-residue anti-parallel beta-sheet motif between residues $_{102}$KKSVAFKKTKK$_{112}$ and $_{140}$ATPVKKAKKKA$_{151}$. Next, the loop 1 region is a 20-residue loop that is closed by the beta-sheet motif discussed above and comprises residues $_{113}$EIKKVATPKKASKPKKAASKA$_{139}$. Loop 1 is very flexible and interacts more strongly with linker α3 (17-32 bp) and transiently with linker L1 (18-23 bp). Such transient DNA-DNA bridging stabilizes a compact chromatosome conformation but allows the last basepairs of both linker DNA segments to remain flexible. Loop 2 is a 24-residue loop ($_{152}$ATPKKAKKPKTVKAKPVKASKPKK$_{175}$) that behaves very similar to the beta motif; this is, it is among the least flexible regions as it interacts very strongly with both linkers L1 and α3 become squeezed in between them right at the DNA crossing point (see contacts in Figure 2B). This is consistent with NMR experiments suggesting that a partially conserved segment in H1.0 Drosophila (corresponding to $_{155}$PKKAKK$_{160}$ in our case) is folded into the nucleosome (9). Finally, the end region formed by the last 19 CTD residues, $_{176}$AKPVKPKAKSSAKRAGKKK$_{194}$ is very flexible and interacts transiently with the nucleosomal DNA and the linker L1.

Supporting Methods

Multiscale Methodology

Given the unstructured and flexible nature of the CTD of H1.0, characterizing its statistical ensemble at high resolution (i.e. atomistic configurations) when bound to the nucleosome and its impact in nanoscale chromatin organization remains challenging for both experiments and computational approaches alike. To address these challenges, we have combined the latest experimental structural data (7, 8) on nucleosome bound-H1 with an advanced multiscale modelling and simulation strategy. At the highest level of resolution, our multiscale approach consists of an extensive set of enhanced sampling atomistic simulations. At the lower-level of resolution, our approach investigates the structural behaviour of 100-nucleosome systems using an updated version of the advanced NYU mesoscale chromatin coarse-grained model. The update developed here consists on a new H1.0 coarse-grain model derived from our atomistic simulations. See detailed description below in Section 2.1.5.

Level 1: Atomistic Simulations

1.1 List of Atomistic Simulations

Table S1: List of atomistic simulations performed for this work.

	System	Force-field	Time	Simulation
1	211bp-Chromatosome + WT LH	Amber99SB-ILDN (36) + parmbsc0 (37) + TIP3P (38)	5 replicas, 1μs per replica	WT-BEMetaD
2	211bp-Chromatosome + WT LH	Amber03ws (39) + parmbsc0 + TIP4P-2005 (40)	5 replicas, 750 ns per replica	WT-BEMetaD
3	211bp-Chromatosome + WT LH	Charmm36M (41) + Charmm36 DNA (42) + TIP3P	5 replicas, 500 ns per replica	WT-BEMetaD
4	Reduced Chromatosome + WT LH	Amber99SB-ILDN + parmbsc0 + TIP3P	5 replicas, 1μs per replica	WT-BEMetaD
5	Reduced Chromatosome + Partial Phosphorylated LH	Amber99SB-ILDN + parmbsc0 + TIP3P	5 replicas, 1μs per replica	WT-BEMetaD
6	Reduced Chromatosome + Fully Phosphorylated LH	Amber99SB-ILDN + parmbsc0 + TIP3P	5 replicas, 1μs per replica	WT-BEMetaD
7	Isolated WT CTD	Amber99SB-ILDN + TIP3P	16 replicas, 200 ns per replica	REST2
8	Isolated Partial Phosphorylated CTD	Amber99SB-ILDN + TIP3P	16 replicas, 200 ns per replica	REST2
9	Isolated Fully Phosphorylated CTD	Amber99SB-ILDN + TIP3P	16 replicas, 200 ns per replica	REST2
10	Isolated NTD	Amber99SB-ILDN + TIP3P	56 replicas, 250 ns per replica	T-REMD

11	211bp-Chromatosome + WT LH Globular Domain	Amber99SB-ILDN + parmbsc0 + TIP3P	500 ns	Unbiased MD
12	211bp-Nucleosome (without LH)	Amber99SB-ILDN + parmbsc0 + TIP3P	500 ns	Unbiased MD

1.2 Model Building

Chromatosome Model: The atomic coordinates for the 211-bp chromatosome with two symmetric 32-bp DNA linker arms were initially extracted from one of the central nucleosomes in the 1ZBB tetra-nucleosome structure (12). The eight histone proteins were then replaced by those from the 1.9 Å resolution 1KX5 structure (13) containing histone tails. The human H1.0 sequence was obtained from the Uniprot Consoritum (14) (ID: P07305) and Modeller (15) was used to create a homology model of the GD of H1.0 with H5 (PDB 4QLC) (7) as the template. This modelled H1.0 GD was positioned on the nucleosome by overlaying it to H5 in the 4QLC structure. The unstructured NTD and CTD of H1.0 were independently built in extended random coil configuration using VMD (16). A standard REMD simulation of this CTD was performed and a random configuration capable of fitting between the linker arms was selected. The NTD and chosen CTD were attached to the previously built H1.0 model using Pymol (17). Finally, a short 1 ns MD simulation of this conformation was performed in the GBSA implicit solvent (18, 19) to condense the terminal domains. This condensed system was then solvated in an octahedral box for the simulations.

Reduced Chromatosome System: The reduced or truncated chromatosome system was built for computational expedience to test effects of phosphorylation on the conformations of CTD within the nucleosome. This was built by removing atoms from the 211-bp nucleosome model. Truncated α3 and L1 linkers were modelled as the terminal 32 bp each of the 211-bp nucleosome. The nucleosomal DNA interacting with DNA was modelled as a 30-bp segment (15 bp each side of the dyad). To maintain the nucleosomal configuration, the bottom two base-pairs of the linker strands were restrained with force constants of 1000 kJ mol^{-1} nm^{-2}. To maintain the curvature of the nucleosomal DNA, the phosphorus atoms within them were restrained with similar force constants. Histone tails H3, H4, and H2B were also included in the model and the last two tail amino acids were restrained at their point of attachments to the histone core. This system was then solvated in an octahedral box.

Isolated NTD: The first 26 residues of H1.0 was considered to constitute the N-terminal domain. The sequence was built in extended conformation using Avogadro (20). This system was then condensed using an initial 1 ns simulation in GBSA implicit solvent. The condensed system was then solvated in a dodecahedron box.

Isolated CTD: The final 98 residues of H1.0 were considered to constitute the C-terminal domain. The conformation of the CTD previously attached to the H1.0 globular domain was independently condensed in a 1 ns simulation in GBSA implicit solvent. This condensed system was then solvated in a dodecahedron box.

1.3 Simulation Setup

The atomistic simulations were performed in Gromacs 5 (21). Short range interactions were modelled using a Lennard-Jones potential with a cut-off of 10 Å. The PME method (22) was used for long-range coulombic interactions with a real-space cut-off of 1.4 nm. The Settle algorithm (23) was used to constrain the bond-lengths of water and P-LINCS was used for all other bonds. Before production runs, all systems were energy minimized using the steepest gradient algorithm and equilibrated for 1 ns each of the NVT and NPT ensembles. The temperatures were maintained using the v-rescale thermostat (24) and pressure was maintained at 1 bar using the Parrinello-Rahman barostat (25). The force fields and water

models used, as well as the length of the different simulations and number of replicas are described in the Table S1. All simulations were done with 150mM of sodium and chlorine ions.

Phosphorylated serine and threonine residues were modelled using the Amber compatible parameters developed by Homeyer et al. (26) and they were introduced into the structure using PyMOL (17). Given that nuclear magnetic resonance (NMR) chemical shifts of the N-H protons in both phosphoserine and phosphothreonine residues show that they are mainly dianionic at pH > 6 (27), their charges were set to −2.

1.4 Enhanced Sampling Methodology

The enhanced sampling simulations were carried out using Gromacs together with Plumed 2.3.0 (28). Further details are given below.

1.4.1 Biased-Exchange Metadynamics Simulations

Well-Tempered (29) Biased-Exchange (30) Metadynamics (31) (BEMetaD) were performed on the full-length linker histone H1.0 bound to either the full 211-bp chromatosome or to the 'reduced' chromatosome described. In BEMetaD simulations, multiple replicas {i} of the system are simulated at the same temperature while being biased along different Collective-Variables (ξi). At regular intervals, the atomic co-ordinates of two random walkers 'a' and 'b' are exchanged with probability

$$P = min\left\{1, exp\left(\frac{1}{k_B T}\left[V_G^a(x^a) + V_G^b(x^b) - V_G^a(x^b) - V_G^b(x^a)\right]\right)\right\}$$

where V_G^i is the history-dependant metadynamics potential along CV *'i'* and x^i are the atomic coordinates of replica *'i'*. The exchanges thus allow each walker to independently diffuse along each CV space unencumbered by minima along correlated CVs.

To sample the conformations of the H1.0 CTD within the nucleosome, five different replicas were used (one unbiased replica and four metadynamics-biased replicas) and exchanges were attempted between them at fixed intervals. Table S2 below summarizes the CVs applied along each of the five replicas. The unbiased replica '1' ($V_G^1 = 0$) is known as the 'neutral' replica.

Table S2: The Metadynamics biasing CVs of the CTD within each of the replicas.

Replica Number	CV
1	None (Unbiased)
2	S_α
3	S_β
4	S_{cont}
5	S_{rg}

The two secondary structure CVs (S_α, S_β) are defined following the work of Pietrucci and Laio (32) as

$$S_{\alpha/\beta} = \sum \frac{1 - \left(\frac{\Delta RMSD}{R_0}\right)^n}{1 - \left(\frac{\Delta RMSD}{R_0}\right)^m}$$

where R_0, n and m are 0.08 nm, 8 and 12 respectively. ΔRMSD is the root mean square difference of six residue segments between the configuration and ideal alpha/beta conformations.

The CV biasing the number of electrostatic contacts (S_{cont}) is defined as

$$S_{cont} = \sum_{i \in H^+} \sum_{j \in O^-} \frac{1 - \left(\frac{\vec{r_i} - \vec{r_j}}{R_0}\right)^n}{1 - \left(\frac{\vec{r_i} - \vec{r_j}}{R_0}\right)^m}$$

where R_0, n and m are 0.2 nm, 8 and 10 respectively. H^+ is the set of positively charged terminal hydrogens in basic R/K residues and O^- is the set of negatively charged Oxygen atoms in the DNA backbone.

The CV S_{rg} biased the radius-of-gyration (Rg) of the Cα atoms of the 98 making up the CTD. This was defined as

$$S_{\mathrm{rg}} = \left(\frac{\sum_i^n m_i |r_i - r_{COM}|^2}{\sum_i^n m_i}\right)^{1/2}$$

where r_i and m_i are the position and mass of atom *i*. r_{COM} is the centre of mass of the CTD Cα atoms.

1.4.2 Replica Exchange with Solute Tempering Simulations

Replica Exchange with Solute Tempering (REST2) simulations (33) were performed to sample the conformations of the disordered C-terminal domain when isolated in solution. The implementation of this REST2 method within Gromacs (21) followed the work of Bussi (34). Briefly, a λ_i parameter is used for each replica '*i*' that scales the Hamiltonian of the solute's (protein) interactions by

- Scaling the charge of solute atoms - $q_i^{pro} = \sqrt{\lambda_i} q^{pro}$.
- Scaling the LJ parameters of solute atoms - $\epsilon_i^{pro} = \lambda_i \epsilon^{pro}$.
- Scaling the 1-4 dihedral interactions - $U_i^{dihed} = \lambda_i U^{dihed}$.

Thus, if the potential energy of the system U_{tot} is divided into its constituent interactions – solute-solute (U_{pp}), solute-solvent (U_{pw}) and solvent-solvent (U_{ww}), they are scaled by factors of T/λ_i, $T/\sqrt{\lambda_i}$ and 1 respectively. Hence, the energy differences between protein conformational changes are scaled while solvent-solvent interactions are unaffected.

In sampling the conformations of the CTD and its phosphorylated states when isolated in solution, 16 replicas geometrically spaced between 300 and 450 K were used. The λ_i of the 16 replicas for scaling their Hamiltonians were calculated as

$$\lambda_i = \frac{T_0}{T_i}$$

where T_0 is 300 K. Exchanges between the replicas were attempted every 10 ps and replicas were simulations for 200 ns each. The initial 50 ns of the trajectory was discarded for equilibration and the remaining trajectory was used for analysis.

1.4.3 Temperature Replica Exchange Simulations

The Temperature Replica-Exchange MD (T-REMD) simulations were performed to sample the conformations of the isolated N-terminal domain. The distribution of temperatures were estimated using the predictor of Patriksson and Van-der-Spoel (35) and an acceptance probability of 20%. This resulted in 56 replicas between the temperatures of 300 and 450 K. The simulations were performed for 250 ns in each replica for a total sampling of 14 μs and exchanges between the replicas were

attempted every 10 ps. After discarding the initial 50 ns, the coordinates from the lowest temperature replicas were considered for analysis

1.5 Trajectory Analysis

1.5.1 Metadynamics Reweighting

In the metadynamics simulations, the addition of history dependant bias potentials precludes a direct ensemble averaging of the system's characteristics as simulation time is without physical meaning. The methodology of Bonomi et al. (43) was thus used to reweight the trajectory frames and subsequently calculate the unbiased equilibrium ensembles. Briefly, the Probability Distribution of the biased system *P(R,t)* can be expressed as

$$P(R,t) = \frac{exp(-\beta[U(R) + V(s(R),t)])}{\int exp(-\beta[U(R) + V(s(R),t)])\, dR}$$

where *U(R)* is the internal potential and *V(s(R),t)* is the metadynamics bias potential. The introduction of the delta function *δ(s – S(R))* and the unbiased probability density function $P_0(R,t)$ allows the expression of the equation as

$$P(R,t) = P_0(R,t) \cdot exp(-\beta[V(s(R),t) - c(t)])$$

where *c(t)* is the time-dependant bias offset defined as

$$c(t) = \frac{1}{\beta} ln \left[\frac{\int exp\big(-\beta F(s)\big)\, ds}{\int exp(-\beta[F(s) + V(s,t)])\, ds} \right]$$

Disregarding this offset, the unbiased probability $P_0(R,t)$ can be then be calculated from the biased probability *P(R,t)* as

$$P_0(R,t) = P(R,t) \cdot exp(\beta[V(s(R),t)])$$

See Bonomi et al. (43) for a complete derivation. These unbiased probabilities $P_0(R,t)$ along each of the replicas were combined using the Weighted Histogram Analysis Method (WHAM) to assign weights *w(t)* for each frame of the concatenated trajectory. The equilibrium average of any system characteristic *O* was then calculated

$$\langle O \rangle = \frac{\sum w_i(t) O_i}{\sum w_i}$$

1.5.2 Secondary Structure Calculation

DSSP (44) implemented within the MDTraj (45) Python library was used to assign secondary structure to the residues. We used a simplified secondary structure system where residues with both alpha- and 3_{10}-helical structures are together labelled α. For the calculation of per-residue secondary structural content, the per-frame O_i was set to 1 if DSSP predicted a helical/beta structure or 0 otherwise.

1.5.3 Terminal Domain Compaction

To independently assess the compaction of the unstructured domains (Figure 2A) and the significance of the change between the bound/unbound states, we compared their R_g to the theoretically calculated values of globular (46) and random-coil (47) proteins. These were calculated as

$$\mathrm{R_g^{glob}(N)} = 2.2\mathrm{N}^{0.38}$$

$$R_g^{coil}(N) = 2.02N^{0.60}$$

where *N* is the number of residues (98 in the case of CTD here).

1.5.4 Calculation of DNA Curvature

The curvature of DNA strands were estimated as a dimensionless quantity following the work of Pasi et al. (48). To do this Curves+ (49) was first used to fit the curvilinear helical axis of the DNA strand as a set of point U_i centred at each base-pair *i* for each trajectory frame.

For each base-pair *i*, two local circles are then fitted across the points $\{U_{i-1}, U_i, U_{i+1}\}$ and $\{U_i, U_{i+1}, U_{i+2}\}$. The radii of these two circles are then calculated as r_i and r_{i+1} respectively. The curvature of the step C_i is then calculated as

$$C_i = \sqrt{\left(\frac{1}{r_i} \times \frac{1}{r_{i+1}}\right)}$$

To normalize this quantity C_i, it is then multiplied by a scaling of 40 to ensure that curvature of the 1KX5 nucleosome structure (13) is calculated as 1. The curvature of the L1/α3 strands were then calculated as the WHAM-weighted mean of the individual C_i of the base-pairs within them.

1.5.5 Clustering Procedure

Clustering was performed using the single-linkage method of clustering within Gromacs. Within this method, a frame *'j'* was assigned to cluster *'i'* if the Root-Mean-Square-Displacement (RMSD) between them was less than 2.5 Å. For the calculation of RMSD, the 98 Cα atoms of the C-terminal domain were considered. The weight of each cluster *'W_i'* was then calculated as

$$W_i = \sum_{j \in i} w_j$$

where 'w_j' is the weight of each frame *'j'* assigned to cluster *'i'*,

Level 2: Coarse-Grained Simulations

To investigate the implications of our all-atom findings in nanoscale chromatin structure, we carried out coarse-grained simulations of 100-nucleosome systems with a uniform nucleosome repeat length of 200 bp that explore the effects of CTD flexibility. For this, we use the NYU coarse-grained chromatin model which is summarized below and detailed in our previous work (50–52) — albeit with an updated H1 description. The NYU model includes several important features of nanoscale chromatin, such as electrostatic interactions, DNA and nucleosome mechanics, structural irregularity, and histone tail flexibility, and averages out other effects like protein/DNA sequence effects, hydrogen bonding, atomistic fluctuations, and solvation.

2.1 Description of CG Model

The components of the model can be briefly described as follows

2.1.1 Nucleosome Core

The nucleosome protein core together with the wrapped DNA (excluding the histone tails) is modelled as a rigid irregular body with 300 Debye-Huckel charges uniformly distributed on the nucleosome molecular surface. The charges are optimized to reproduce the full atom electric field around the nucleosome by the Discrete Surface Optimization (DiSCO) algorithm (53) that solves the nonlinear Poisson-Boltzmann equation.

2.1.2 Histone Tails

The ten histone tails protruding out of each core (N-termini of H2A, H2B, H3, H4 and C-terminus of H2A) are modelled as flexible chains of beads. Each bead is comprised of 5 amino-acid residues and is rigidly attached to the parent core. The stretching and bending flexibility constants of each tail inter-bead segment are modelled by harmonic potentials with parameters developed to mimic atomistic flexibilities (50, 54). The charges of the beads are modelled to equal those of their constituent amino acids.

2.1.3 Linker DNA

The DNA connecting consecutive nucleosomes is treated as a chain of spherical beads that have a salt-concentration dependant charge parameterized using the method of Stigter (55). For describing the mechanical properties of DNA, the wormlike-chain (WLC) chain model (56, 57) of Jian et al. (58, 59) was used. The equilibrium inter-bead DNA segment is modelled at 3 nm (9 bp). The entering and exiting DNA are modelled with an equilibrium angle to the nucleosome of 108˚ corresponding to a wrapping of 147 base-pairs.

2.1.4 Solvent and Ionic Environment

The solvent around the oligonucleosomes is modelled implicitly as a continuum. The screening of electrostatic interactions due to the presence of monovalent ions in solution (0.15 M NaCl) is treated using a Debye-Hückel potential (screening length 1.27 nm^{-1}) (50).

2.1.5 Multiscale Mapping of Linker Histone Model from this Work

In this work, we took advantage of our atomistic statistical ensembles for the nucleosome-bound H1 to developed a more realistic coarse-grained modelled based on this behavior. We focused on the human linker histone H1.0 with a resolution of one bead per five amino-acid residues, and centred each bead at the C_α atom of the central amino acid. This consisted of 37 beads: 4 beads for the NTD, 14 beads for the GD, and 19 beads for the CTD. Each bead of the GD contained one pseudo-charge optimized to reproduce the full atom electric field with the DiSCO algorithm (53) using as the reference configuration the highest populated structure in our full-nucleosome bound H1 atomistic BEMetaD simulations (neutral replica). For beads representing disordered protein regions, we instead defined the bead charges as the sum of the constituent charges (average charge per bead of +2.4e). Using again the configuration of H1 from the highest populated cluster from our atomistic simulations, we rigidly attached the N- and C-terminal tails to the GD. Because the secondary structure of the globular domain was conserved throughout our atomistic simulations, this domain was kept rigid. For the NTD and CTD, we focus on the C_α atom of the central residue that would correspond to each bead, and evaluated the bond and angle distributions from our full-nucleosome bound BEMetaD simulations (neutral replica). To then map the atomistic behavior to our coarse-grained model, we searched for an inter-bead potential that would reproduce the obtain distributions. For all cases, a Gaussian function seemed an adequate fit, which allowed us to approximate the stretching and bending potentials as harmonic and derive the inter-bead potential parameters with a simple Boltzmann inversion (see Figures S8 and S9). Our resulting linker histone force-field is now non-uniform, i.e., it has parameters that depend on the identity of the bead:

$$E_S = \sum_{i=1}^{N-1} \frac{1}{2} k_i^s \left(l_i - l_i^{eq}\right)^2$$

$$E_b = \sum_{i=1}^{N-2} \frac{1}{2} k_i^b \left(\theta_i - \theta_i^{eq}\right)^2$$

l_i^{eq} and k_i^s are the stretching equilibrium value and force constant between beads i and $i+1$, and θ_i^{eq} and k_i^b are the bending equilibrium value and force constant between

beads i, $i+1$ and $i+2$. These distributions and parameters are provided in Figures S8 and S9 below.

In addition, to model less flexible CTD systems ('LessFlex'), we multiply the stretching and bending force-constants by 10, and to model more flexible systems ('MoreFlex'), we divide them by 10. We also model a control case that we term 'Symmetric', in which model the CTD as a homopolymer instead; that is, for all beads, independently of their identity, we set: $k_s = 10$ kcal/mol nm^2, $k_b = 1$ kcal/mol rad^2, $l_{eq} = 1.5$ nm, and $\theta_{eq} = 110°$.

We also included an excluded volume term (E_{ev}), to avoid overlap between non-consecutive H1 beads and with other chromatin components:

$$E_{ev} = \sum_{i=1}^{N-2} \sum_{j>i+1}^{N} k_{ev} \left[\left(\frac{\sigma_{cc}}{r_{ij}} \right)^{12} - \left(\frac{\sigma_{cc}}{rij} \right)^{6} \right]$$

Here, rij is the distance between beads i and j, $k_{ev} = 0.001 k_B T$ as in the rest of the model, and $\sigma_{H1-H1} = 1.8$ nm for H1-H1 beads, $\sigma_{H1c} = 1.8$ nm for H1-core beads, $\sigma_{H1L} = 2.7$ nm for H1-linker DNA, and $\sigma_{H1c} = 1.8$ nm for H1-histone tail. Finally, we also included a Debye-Hückel potential for electrostatics:

$$E_c(i,j,) = \frac{q_i q_j}{4\pi\epsilon_0\epsilon_r r_{ij}} \exp\left(-\kappa r_{ij}\right).$$

Here i is a linker histone bead and j is a bead of an interacting chromatin components, q_i and q_j are the effective charges of the chromatin components, κ is the inverse Debye length, ϵ_0 is the electric permittivity of vacuum and ϵ_r is the relative permittivity of the medium (set to 80).

2.1.6 Phosphorylated Linker Histone Terminal Domains

Similar to the above described methodology for the parameterization of the WT LH terminal domains, CG parameters for the two phosphorylated cases were also obtained from the atomistic simulations. As described above, the charges of the beads is the sum of the charges of the constituent amino acids. With the WT H1.0 CTD possessing a charge of +42e, and the partially phosphorylated case a net charge of +32e. In the fully phosphorylated case, all 13 Ser/Thr residues were considered phosphorylated and the CTD thus had a composite charge of +16e. As an approximation, we modeled the fully phosphorylated and partial phosphorylated versions with 40% and 70%, respectively, of the charge of the WT protein.

2.2 Monte-Carlo Simulation Algorithm

The Monte Carlo simulations of 100 nucleosomes are performed at a constant temperature selecting randomly from the five different moves described below. The first three MC moves are global pivot, local translation and local rotation moves which together focus on the conformational sampling of the main oligonucleosome chain.

The global pivot move is implemented by randomly choosing one linker bead/nucleosome core and a random axis passing through the chosen component. The shorter part of the oligonucleosome about this axis is rotated by an angle chosen from a uniform distribution within a range so that the acceptance probability is ~25%.

The local translation/local rotation moves are implemented in a similar manner by selecting a random oligonucleosome component (linker bead/nucleosome core) and a random axis passing through the component. The component is then moved along/rotated around the chosen axis by a distance/angle sampled from a uniform distribution chosen within a range so that the acceptance probability is ~25%.

The fourth tail regrowth move samples flexible histone tail conformations based on the configurational bias Monte-Carlo method (60). The move randomly selects a 'flexible' histone tail chain and regrows it bead-by-bead using the Rosenbluth method (61). To prevent the histone tails from penetrating the nucleosome core, the volume enclosed within the

nucleosome surface is discretized and any trial configurations that place the beads within this volume are rejected.

The fifth linker histone move is a local translation move of its tail beads. A linker histone tail bead is selected at random. The bead is then moved in a random direction by a distance sampled from a uniform distribution chosen within a range so that the acceptance probability is ~25%.

The five pivot, translation, rotation, linker histone and tail regrowth moves are attempted with probabilities of 0.2, 0.1, 0.1, 0.2 and 0.4 respectively.

2.3 Coarse Grained Simulations

With the above-described modelling setup and Monte Carlo algorithm, we sample configurations of 100-nucleosome chromatin fibers with one H1 molecule per nucleosome and an uniform repeat length of 200-bp. All simulations were performed at 298 K and 150 mM NaCl. Each simulation set included 12 trajectories covering the deviations from -12˚ to +12˚ about the mean DNA twist angle as done previously (62). Each simulation trajectory was run for 100 million MC steps with the last 10 million steps were used for statistical analysis. Convergence of the simulations is reached well before 60 million MC steps as shown by Bascom et al. (4). As before (62), for the initial configurations, we use idealized zigzag conformations for the oligonucleosomes. Additional model parameters are provided in Tables S1-S4 of ref. (62).

2.4 Analysis Measurements

2.4.1 Inter-Nucleosome Interactions

The matrices of internucleosome interactions $I'(i,j)$ describe the fraction of MC iterations that nucleosomes i and j are in contact with one another. Each matrix element is defined as:

$$I'(i,j) = \mathrm{mean}\left[\delta_{i,j}(M)\right]$$

where M is the MC configurational frame, and the mean is calculated over converged MC frames used for statistical analysis, where,

$$\delta_{i,j}(M) = \begin{cases} 1 & \text{if cores } i \text{ and } j \text{ are } '\text{in contact}' \text{at MC frame } M \\ 0 & \text{otherwise} \end{cases}$$

At a given MC step M we consider nucleosomes i and j to be in contact if the shortest distance between the tail-beads directly attached to i and the tail-beads or core-charges of core j is smaller than a cut-off value of 1.8 nm.

2.4.2 Calculation of Sedimentation Coefficients

The sedimentation coefficient (S_N) of a given oligonucleosome array conformation was calculated as done in our previous work of Collepardo-Guevara and Schlick (52, 63). The S_N is calculated from the set of inter-nucleosome distances R_{ij} as

$$\frac{S_N}{S_1} = 1 + \frac{R_1}{N}\sum_i \sum_j \frac{1}{R_{ij}}$$

where S_1 is the sedimentation co-efficient of a mononucleosome and R_1 is 5.5 nm.

Supporting Figures

Figure S1

Interactions of the DNA strands with the four loop regions of the C-terminal domain from BEMD simulations with three force-field combinations. A contact was assumed if any non-hydrogen atom of the base-pair was within 3.4 Å of a non-hydrogen CTD atom. Base-pairs for the nucleosomal DNA are numbered from -15 to +15 with 0 being the central dyad base-pair.

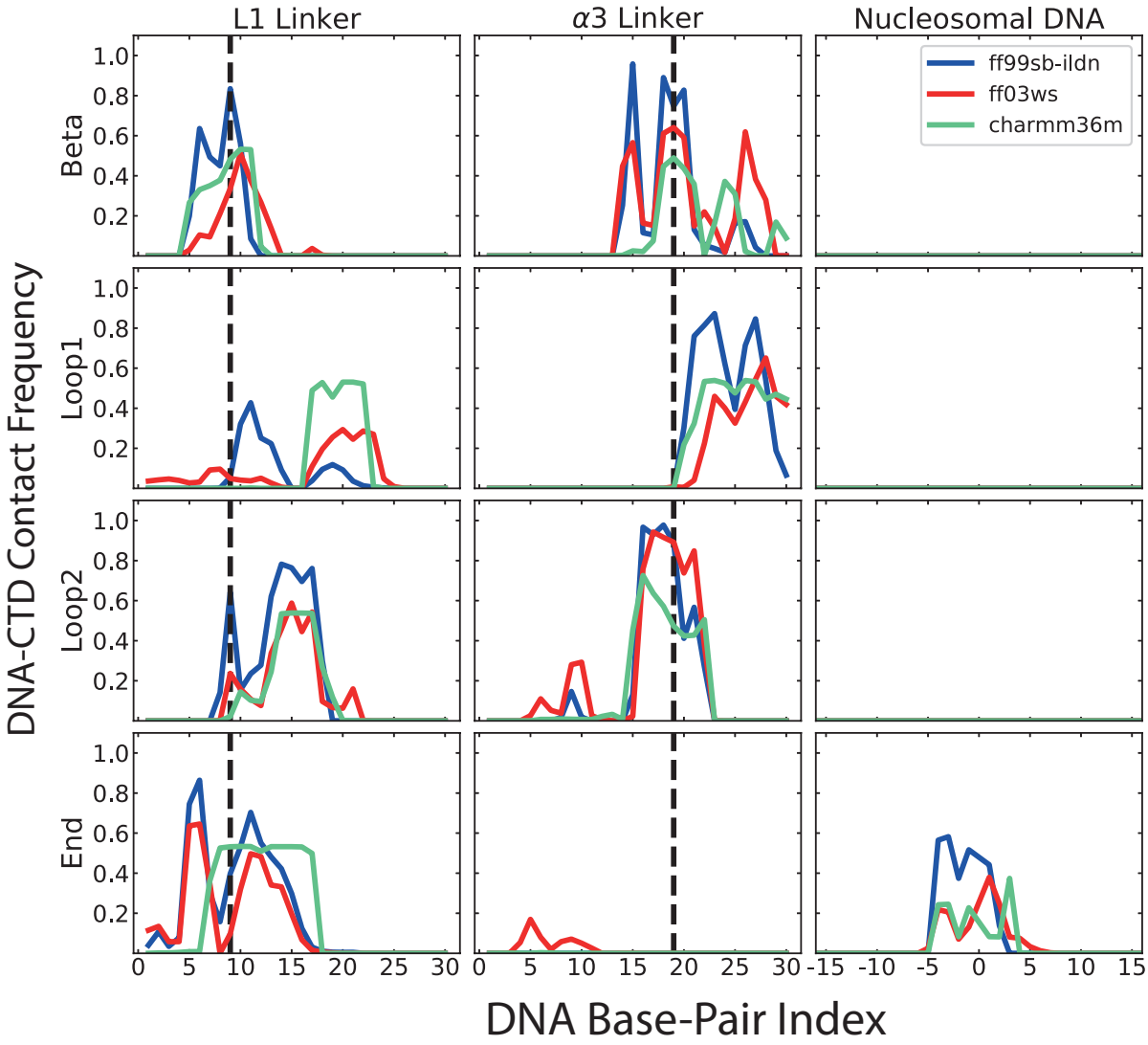

Figure S2
(A) Snapshot of the most heavily weighted cluster of the linker histone N-terminal domain from the BE-Well Tempered Metadynamics simulation. The disordered region was clustered using the single-linkage clustering within Gromacs and a cut-off of 0.25 nm. **(B)** The weighted per-residue secondary structure of the amino-terminal domain from the BE-Well Tempered Metadynamics simulation compared to that from T-REMD simulations isolated in solution.

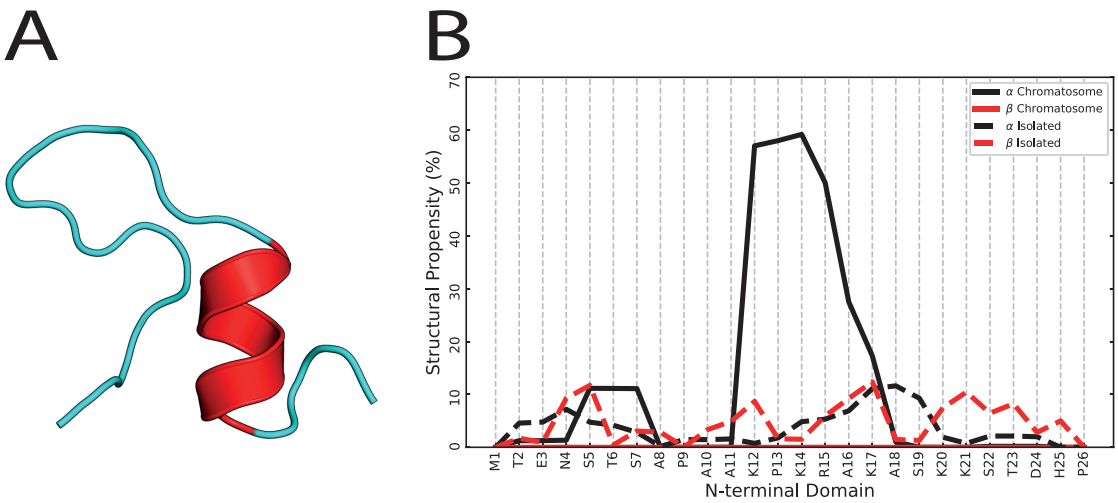

Figure S3

(A) The orientation of the H1.0 globular domain compared between the BE-MetaD simulations with the unstructured terminal domains (purple) and from the 5NL0 (8) crystallographic structure (green). The alignments were generated by aligning 20 base-pairs around dyad. The α3 helix and L1 linker of the LH are highlighted. **(B)** The per-residue interactions of the amino-terminal, globular and carboxyl-terminal domains of the H1.0 linker histone with the L1, α3 and nucleosomal DNA. A contact was assumed if a non-hydrogen atom of the residue was within 3.4 Å of a non-hydrogen DNA atom. The contacts within the globular domain of H1 identified to mediate nucleosomal binding through ITC (7)/FRAP (64) experiments are marked with a '*'.

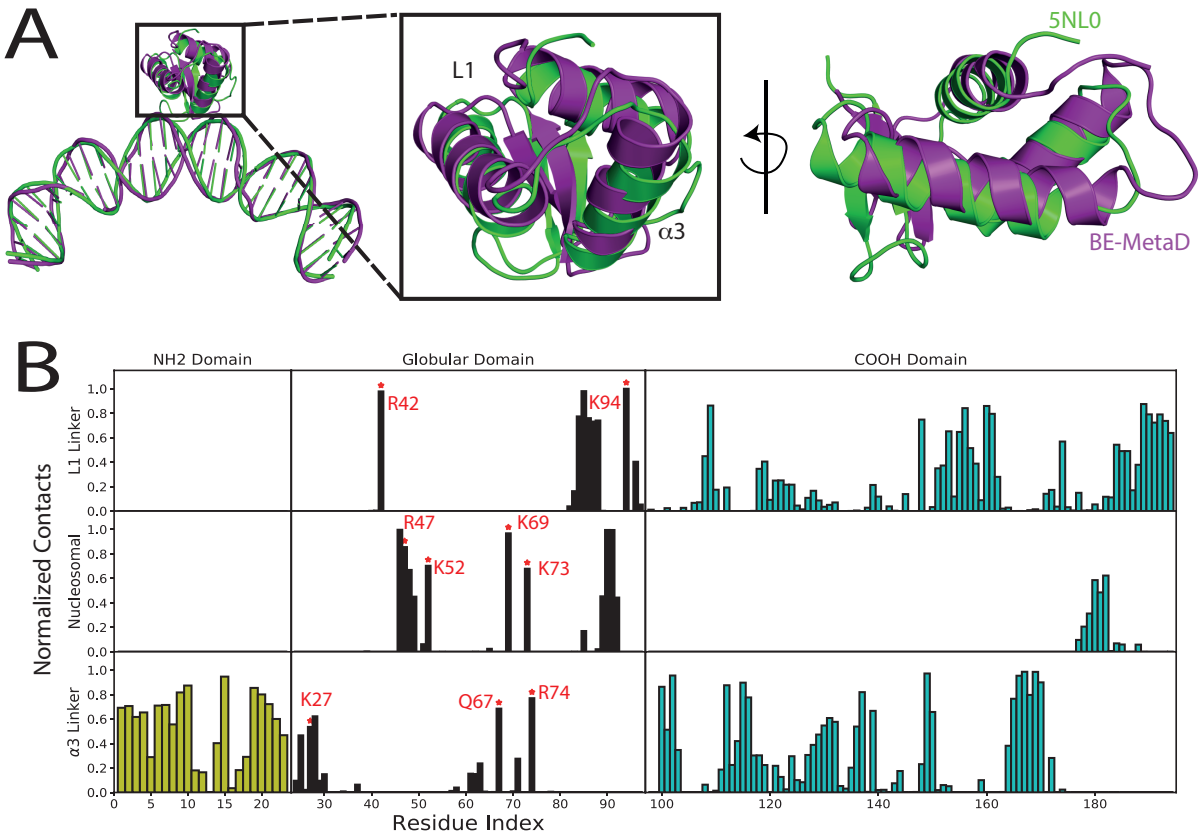

Figure S4

Inter-basepair distances between the two linker arms showing the formation of a symmetric (globular) or asymmetric (full H1.0) topology of linker DNA arms in simulations of the nucleosome with: (top left) only the H1.0 globular domain bound and the ff99sb-ildn force field, (top right) the full H1.0 bound and ff99sb-ildn, (bottom left) the full H1.0 bound and ff03ws, and (bottom right) the full H1.0 and charmm36m. The figure also shows that the asymmetry found for the full H1.0 case is force-field independent.

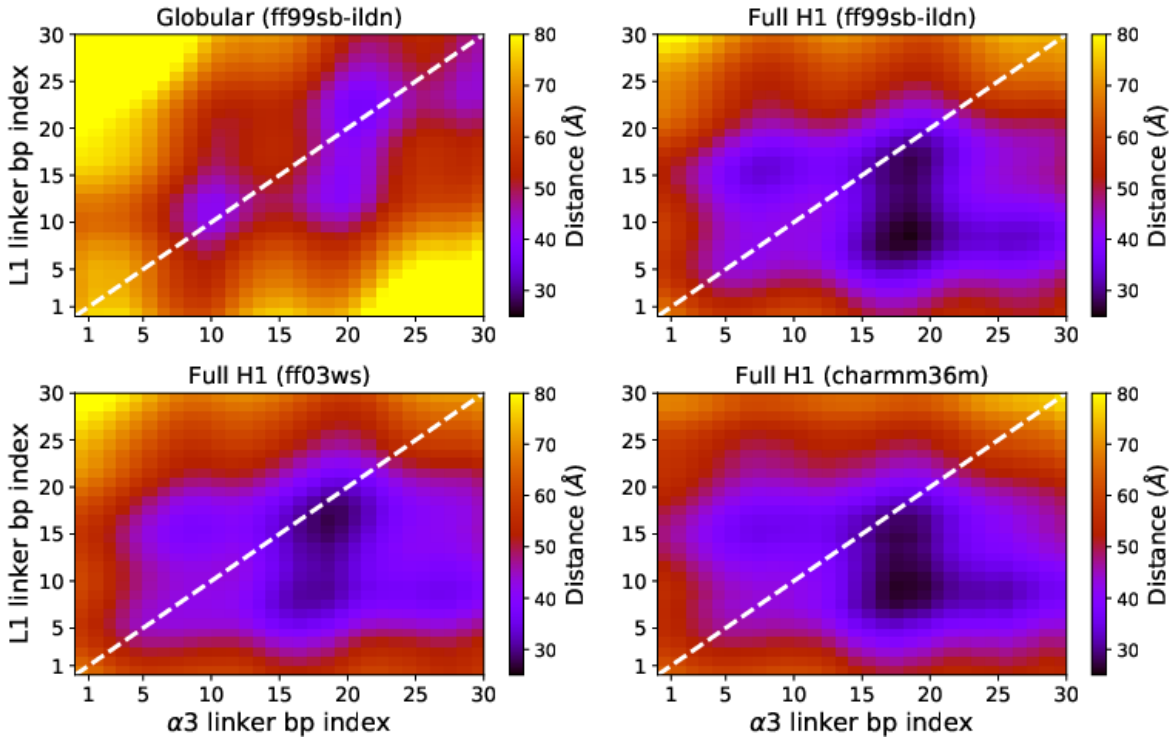

Figure S5

Distribution of all-atom pseudo-bonds and derived coarse-grained potential parameters. We start by partitioning the full H1.0 protein into beads, each comprising 5 consecutive amino acids (e.g. residues 1-5 make bead 1, residues 6-10 make bead 2, and residues 11-15 make bead 3). We then define C^i_{bead} as the C_α of the middle amino acid in the i^{th} bead (e.g. C^1_{bead}, C^2_{bead}, and C^3_{bead}, are the 3rd, 8th, and 13th C_αs, respectively), and compute the distribution of distances between C^i_{bead} and C^{i+1}_{bead} from the neutral replica of our all-atom nucleosome-bound BEMetaD simulations. These distributions are shown below for the NTD and CTD with blue circles. We then fit a Gaussian distribution (shown in with a red line) and by simple Boltzmann inversion we calculate from there the bead-dependent parameters for the heteropolymer stretching potential (force constant, k^i_s, and equilibrium values l^i_{eq}).

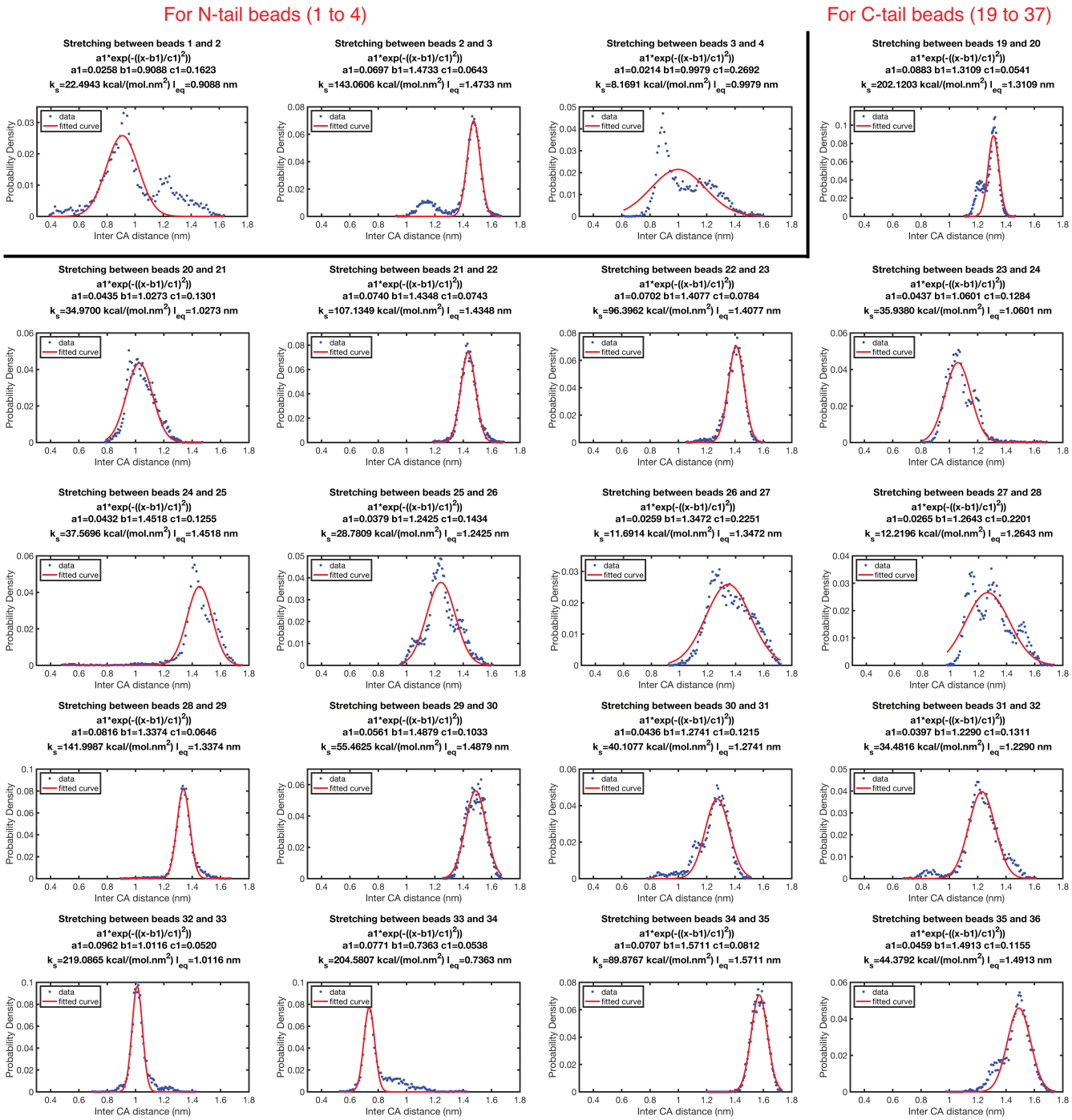

Figure S6

Distribution of all-atom pseudo-angles and derived coarse-grained potential parameters. For the different beads (see caption of Figure S8) we also compute the distribution of angles between C^{i}_{bead}, C^{i+1}_{bead} and C^{i+2}_{bead} from the neutral replica of our all-atom nucleosome-bound BEMetaD simulations. These distributions are shown below for the NTD and CTD with blue circles. We then fit a Gaussian distribution (shown in with a red line) and by simple Boltzmann inversion we calculate from there the bead-dependent parameters for the heteropolymer bending potential (force constant, k^{i}_{b}, and equilibrium values θ^{i}_{eq}).

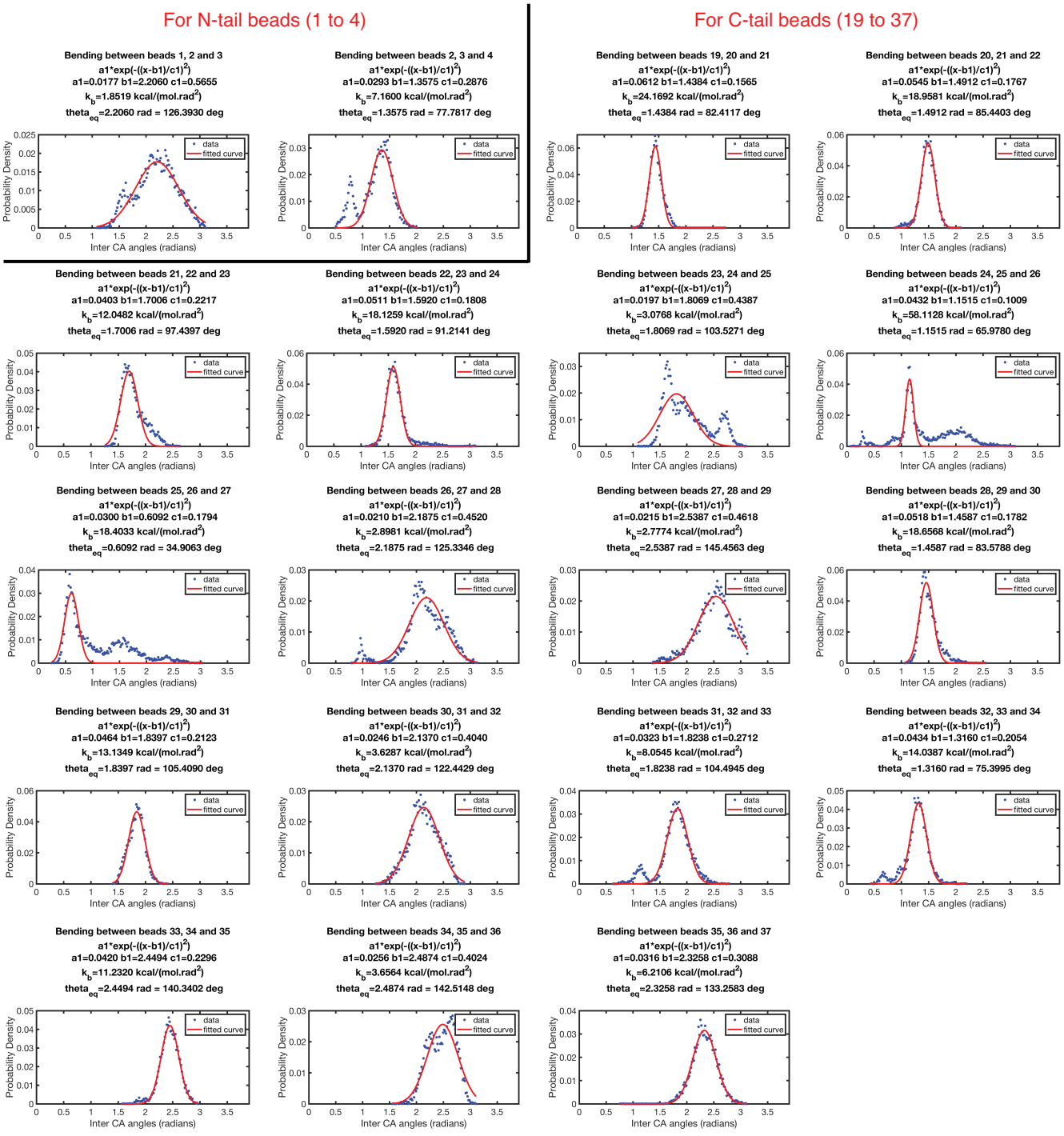

Figure S7

Chromatin end-to-end distance (top) and fiber length (bottom) for 100-nucleosome systems with one H1 bound to each nucleosomes for all the different H1 CTD models explored in this work.

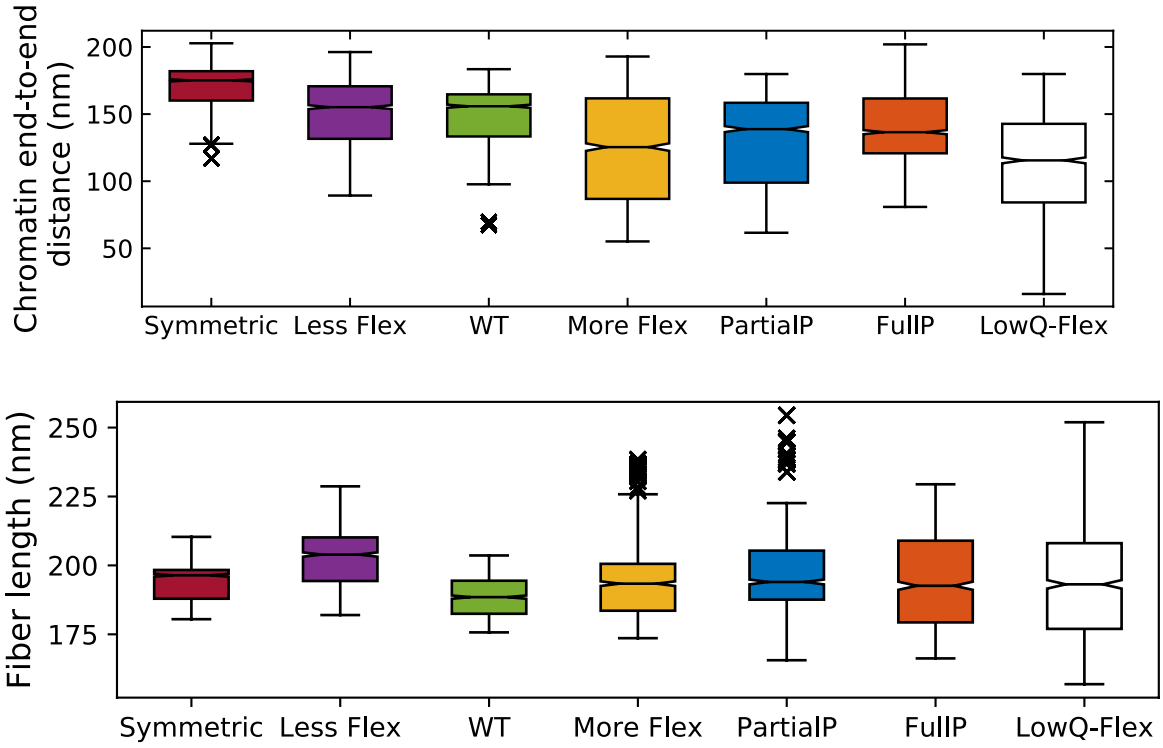

Figure S8

Correlation function between the vectors tangent to the chromatin fiber axis at position zero (t_0) and a tangent vector at a distance s away (t_s) along the contour of the fiber axis plotted as a function of the contour length and computed for each of the different chromatin systems we simulate. The correlation functions decay in a non-exponential manner for all systems, with the decay being slower than exponential at short contour lengths and increasing as the nucleosome-nucleosome linear separation grows. This might indicate that the coupling of the internal chromatin degrees of freedom and the formation/breakage of numerous and highly diverse attractive internucleosome interactions lead to a complex behavior where the local stiffness of chromatin is not well described by the wormlike chain model within the length scales we can access with our simulations. In addition, we note that our chromatin systems are short (~150-250 nm; Figure S7) in comparison with the estimated persistence length of chromatin (~170 to 220 nm;) (65). Despite this, we observe a much faster decay of the correlation functions with contour length for the chromatin systems that exhibit larger fluctuations in their geometrical fiber descriptors (i.e., LowQ-Flex ~ FullP ~ ParP > More Flex >> WT ~ Less Flex > Symmetric), consistent with greater flexibility.

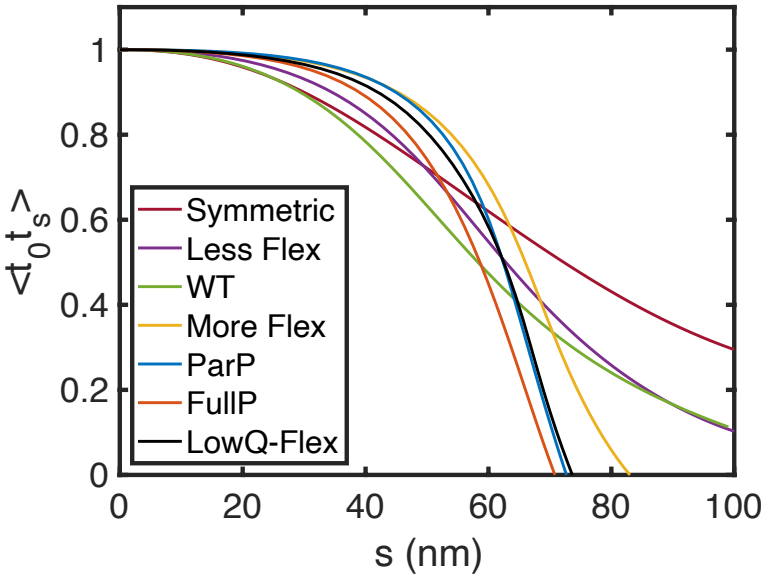

Figure S9

Probability of loop formation as a function of the loop size measured by the fraction of chromatin configurations that exhibit contacts among nucleosomes that are linearly separated by the indicated loop length. Each panel show the results for the different systems we simulate: (a) Symmetric, (b) Less Flex, (c) WT, (d) More Flex, (e) PartialP, (f) FullP and (g) LowQ-Flex. Note that only systems (e), (f), and (g) have a non-zero probability of forming full loops in which the first and last nucleosome (separated by 20kb) contact each other. Hence, only these three systems are expected to have non-zero J-factors; the number above the 20kb datapoint for these cases shows the median of the probability of forming full loops.

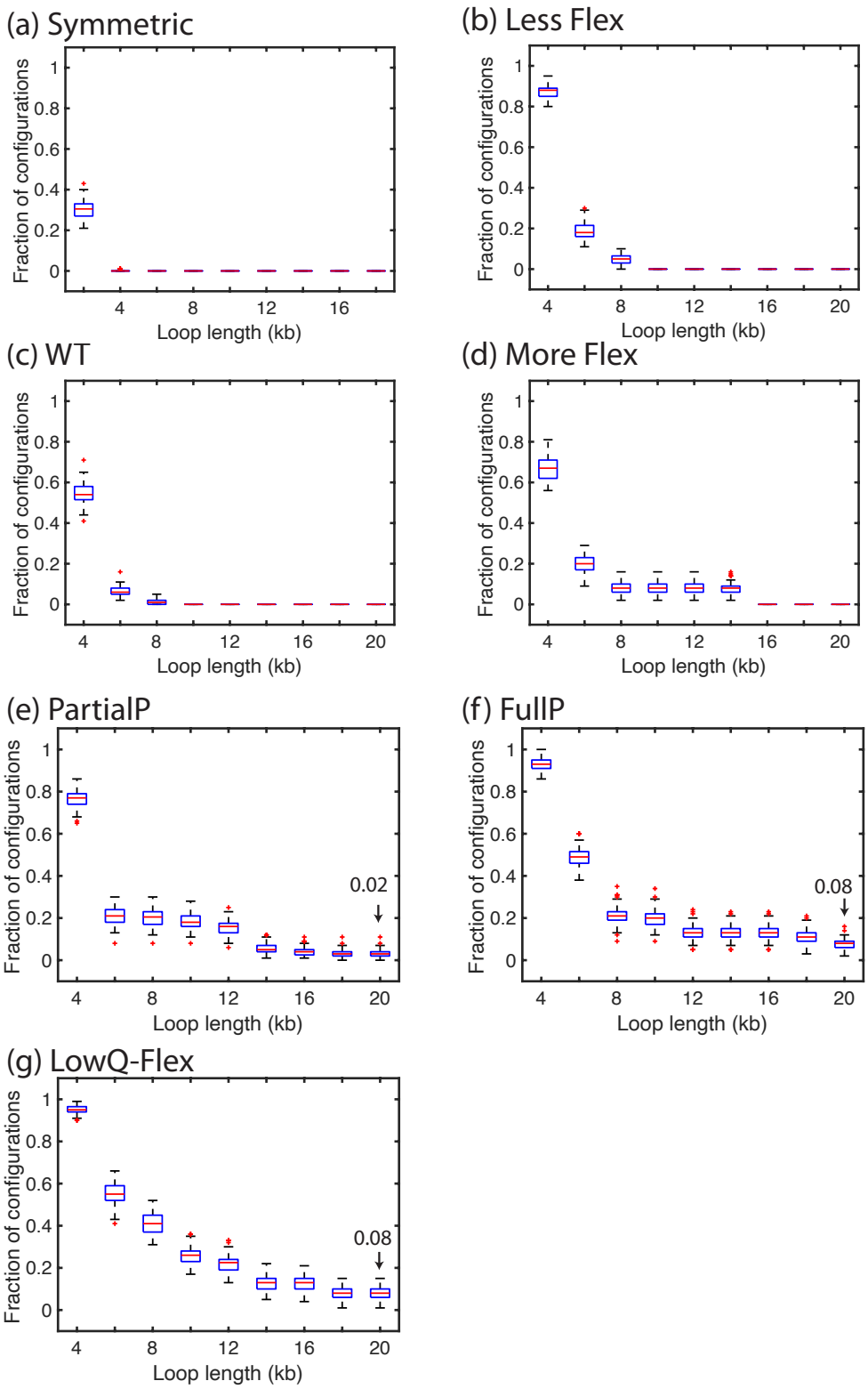

Figure S10

Serine/Threonine sites within the H1.0 CTD modelled in the phosphorylated state within the partially phosphorylated case. The locations of these sites are depicted in the context of the four CTD sub-regions with distinct interaction patterns.

Figure S11

Variations to the uneven patterns of interactions between the three LH domains and DNA regions due to differences in the phosphorylation states of the CTD. A contact was assumed if a non-hydrogen atom of the base-pair was within 3.4 Å of a non-hydrogen protein atom. The interactions of the extended partially-phosphorylated CTD with the L1 linker is highlighted in a red box.

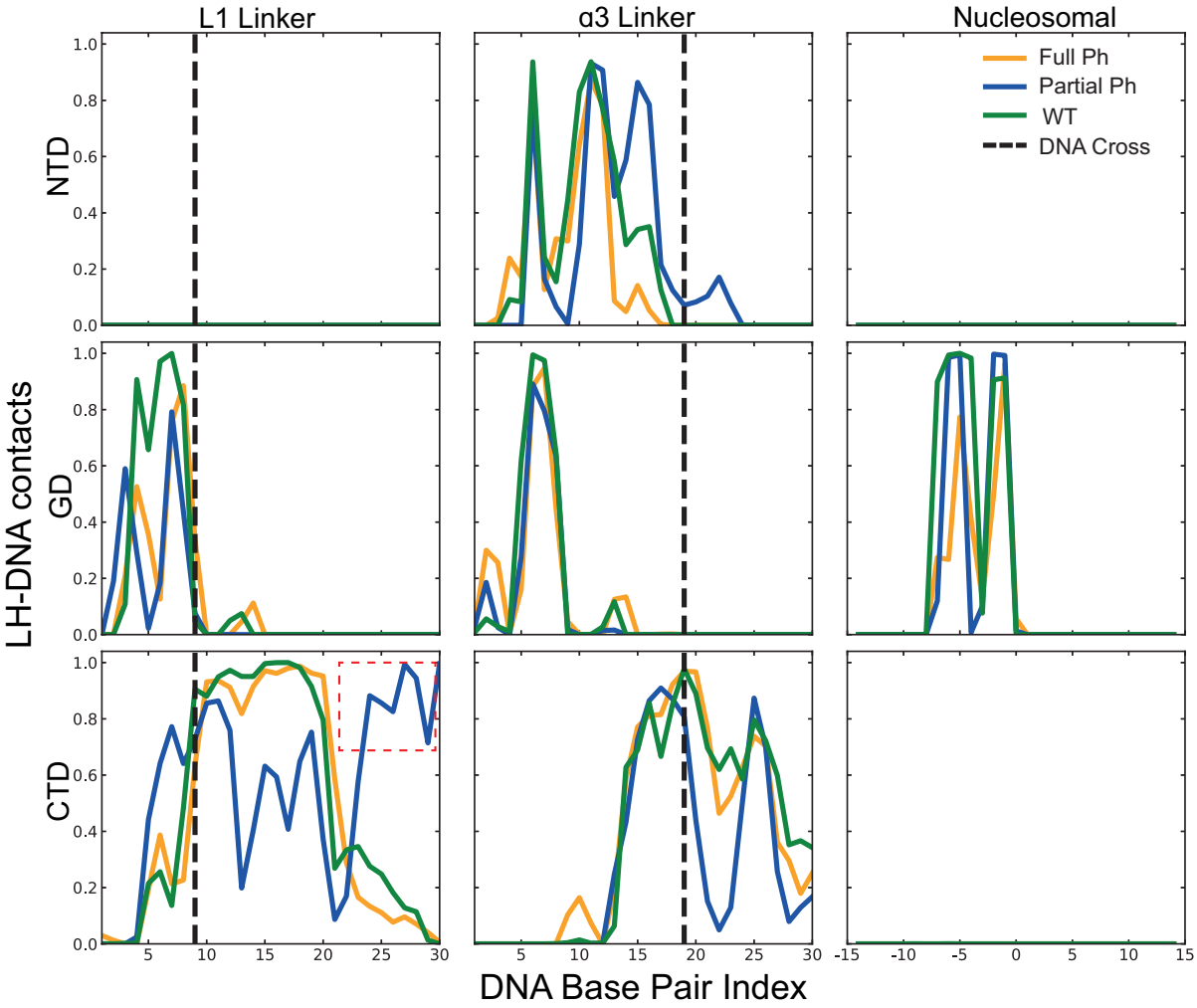

Figure S12

Variations to the intra-CTD interactions due to differences in the phosphorylation states. The hyperphosphorylated CTD adopts a collapsed conformation with higher frequency of intra-protein contacts similar to the WT, while the partially phosphorylated CTD is in an extended conformation with decreased intra-protein interactions.

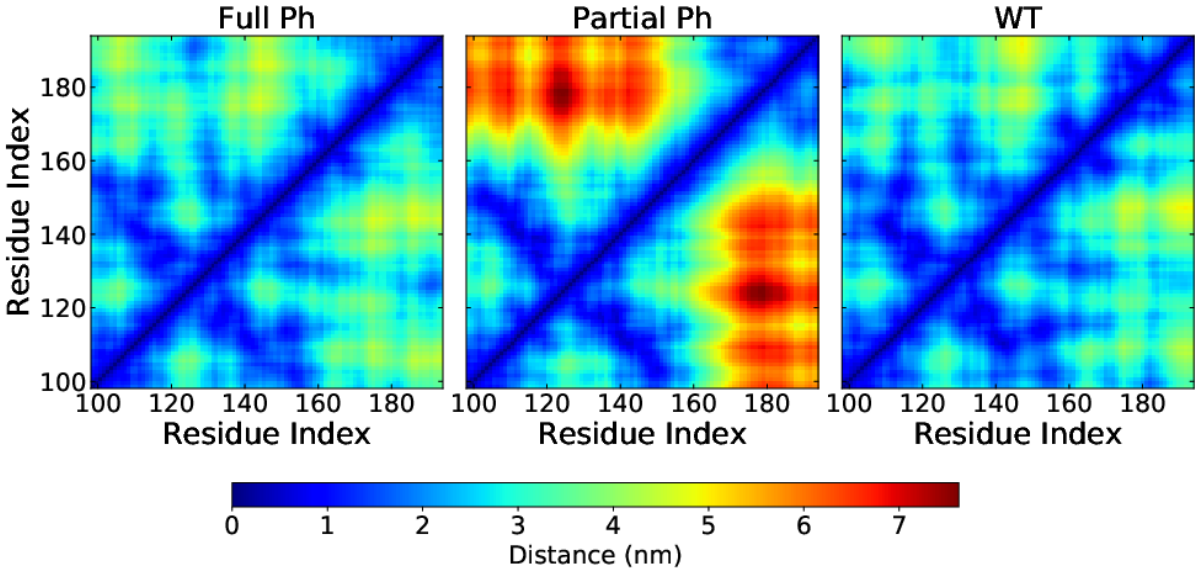

References

1. Oberg C, Belikov S (2012) The N-terminal domain determines the affinity and specificity of H1 binding to chromatin. *Biochemical and Biophysical Research Communications* 420(2):321–324.
2. Allan J, Mitchell T, Harborne N, Bohm L, Crane-Robinson C (1986) Roles of H1 domains in determining higher order chromatin structure and H1 location. *Journal of Molecular Biology* 187(4):591–601.
3. Ramakrishnan V (1997) Histone H1 and chromatin higher-order structure. *Critical Reviews in Eukaryotic Gene Expression* 7(3):215–230.
4. Bascom GD, Sanbonmatsu KY, Schlick T (2016) Mesoscale Modeling Reveals Hierarchical Looping of Chromatin Fibers Near Gene Regulatory Elements. *Journal of Physical Chemistry B* 120(33):8642–8653.
5. Fyodorov D V., Zhou BR, Skoultchi AI, Bai Y (2017) Emerging roles of linker histones in regulating chromatin structure and function. *Nature Reviews Molecular Cell Biology* 19(3):192–206.
6. Zhou BR, et al. (2016) A Small Number of Residues Can Determine if Linker Histones Are Bound On or Off Dyad in the Chromatosome. *Journal of Molecular Biology* 428(20):3948–3959.
7. Zhou BR, et al. (2015) Structural Mechanisms of Nucleosome Recognition by Linker Histones. *Molecular Cell* 59(4):628–638.
8. Bednar J, et al. (2017) Structure and Dynamics of a 197 bp Nucleosome in Complex with Linker Histone H1. *Molecular Cell* 66(3):384–397.
9. Zhou B-R, et al. (2013) Structural insights into the histone H1-nucleosome complex. *Proceedings of the National Academy of Sciences of the United States of America* 110(48):19390–19395.
10. Song F, et al. (2014) Cryo-EM study of the chromatin fiber reveals a double helix twisted by tetranucleosomal units. *Science* 344(6182):376–380.
11. Perišić O, Portillo-Ledesma S, Schlick T (2019) Sensitive effect of linker histone binding mode and subtype on chromatin condensation. *Nucleic acids research* 47(10):4948–4957.
12. Schalch T, Duda S, Sargent DF, Richmond TJ (2005) X-ray structure of a tetranucleosome and its implications for the chromatin fibre. *Nature* 436(7047):138–141.
13. Davey CA, Sargent DF, Luger K, Maeder AW, Richmond TJ (2002) Solvent mediated interactions in the structure of the nucleosome core particle at 1.9 A resolution. *Journal of Molecular Biology* 319(5):1097–1113.
14. Apweiler R, et al. (2004) UniProt: The Universal Protein knowledge base. *Nucleic Acids Research* 32:115–119.
15. Sali A, Blundell TL (1993) Comparative protein modelling by satisfaction of spatial restraints. *Journal of Molecular Biology* 234(3):779–815.
16. Humphrey W, Dalke A, Schulten K (1996) VMD: visual molecular dynamics. *Journal of Molecular Graphics* 14(1):33–38.
17. Schrödinger LLC (2002) The PyMOL Molecular Graphics System.
18. Onufriev A, Bashford D, Case DA (2000) Modification of the Generalized Born Model Suitable for Macromolecules. *Journal of Physical Chemistry B* 104(15):3712–3720.
19. Onufriev A, Bashford D, Case DA (2004) Exploring Protein Native States and Large-Scale Conformational Changes with a Modified Generalized Born Model. *Proteins: Structure, Function and Genetics* 55(2):383–394.
20. Hanwell MD, et al. (2012) Avogadro : an advanced semantic chemical editor , visualization , and analysis platform. *Journal of Cheminformatics* 4(17):1758–2946.
21. Abraham MJ, et al. (2015) Gromacs: High performance molecular simulations through multi-level parallelism from laptops to supercomputers. *SoftwareX* 1(2):19–25.
22. Essmann U, et al. (1995) A smooth particle mesh Ewald method. *The Journal of Chemical Physics* 103(19):8577–8593.
23. Miyamoto S, Kollman PA (1992) Settle: An analytical version of the SHAKE and RATTLE algorithm for rigid water models. *Journal of Computational Chemistry* 13(8):952–962.
24. Bussi G, Donadio D, Parrinello M (2007) Canonical sampling through velocity rescaling. *Journal of Chemical Physics* 126(1). doi:10.1063/1.2408420.
25. Parrinello M, Rahman A (1981) Polymorphic transitions in single crystals: A new molecular dynamics method. *Journal of Applied Physics* 52(12):7182–7190.
26. Homeyer N, Horn AHC, Lanig H, Sticht H (2006) AMBER force-field parameters for phosphorylated amino acids in different protonation states: Phosphoserine, phosphothreonine, phosphotyrosine, and phosphohistidine. *Journal of Molecular Modelling* 12(3):281–289.
27. Lee KK, et al. (2008) Site-selective intramolecular hydrogen-bonding interactions in phosphorylated serine and threonine dipeptides. *Journal of Physical Chemistry B* 112(51):16782–16787.
28. Tribello GA, Bonomi M, Branduardi D, Camilloni C, Bussi G (2014) PLUMED 2: New feathers for an old bird. *Computer Physics Communications* 185(2):604–613.
29. Barducci A, Bussi G, Parrinello M (2008) Well-tempered metadynamics: A smoothly converging and tunable free-energy method. *Physical Review Letters* 100(2). doi:10.1103/PhysRevLett.100.020603.
30. Piana S, Laio A (2007) A Bias-Exchange Approach to Protein Folding. *The Journal of Physical Chemistry B* 111(17):4553–4559.
31. Laio A, Parrinello M (2002) Escaping free-energy minima. *Proceedings of the National Academy of Sciences of the United States of America* 99(20):12562–12566.

32. Pietrucci F, Laio A (2009) A collective variable for the efficient exploration of protein beta-sheet structures: Application to SH3 and GB1. *Journal of Chemical Theory and Computation* 5(9):2197–2201.
33. Wang L, Friesner RA, Berne BJ (2011) Replica exchange with solute scaling: A more efficient version of replica exchange with solute tempering (REST2). *Journal of Physical Chemistry B* 115(30):9431–9438.
34. Bussi G (2014) Hamiltonian replica exchange in GROMACS: A flexible implementation. *Molecular Physics* 112(3–4):379–384.
35. Patriksson A, van der Spoel D (2008) A temperature predictor for parallel tempering simulations. *Physical Chemistry Chemical Physics* 10(15):2073–2077.
36. Lindorff-Larsen K, et al. (2010) Improved side-chain torsion potentials for the Amber ff99SB protein force field. *Proteins: Structure, Function and Bioinformatics* 78(8):1950–1958.
37. Pérez A, et al. (2007) Refinement of the AMBER force field for nucleic acids: Improving the description of α/γ conformers. *Biophysical Journal* 92(11):3817–3829.
38. Jorgensen WL, Chandrasekhar J, Madura JD, Impey RW, Klein ML (1983) Comparison of simple potential functions for simulating liquid water. *Journal of Chemical Physics* 79(2):926–935.
39. Best RB, Zheng W, Mittal J (2014) Balanced protein-water interactions improve properties of disordered proteins and non-specific protein association. *Journal of Chemical Theory and Computation* 10(11):5113–5124.
40. Abascal JLF, Vega C (2005) A general purpose model for the condensed phases of water: TIP4P/2005. *Journal of Chemical Physics* 123(23). doi:10.1063/1.2121687.
41. Huang J, et al. (2016) CHARMM36m: An improved force field for folded and intrinsically disordered proteins. *Nature Methods* 14(1):71–73.
42. Hart K, et al. (2012) Optimization of the CHARMM additive force field for DNA: Improved treatment of the BI/BII conformational equilibrium. *Journal of Chemical Theory and Computation* 8(1):348–362.
43. Bonomi M, Barducci A, Parrinello M (2009) Reconstructing the equilibrium boltzmann distribution from well-tempered metadynamics. *Journal of Computational Chemistry* 30(11):1615–1621.
44. Kabsch W, Sander C (1983) Dictionary of protein secondary structure: pattern recognition of hydrogen-bonded and geometrical features. *Biopolymers* 22(12):2577–2637.
45. McGibbon RT, et al. (2015) MDTraj: A Modern Open Library for the Analysis of Molecular Dynamics Trajectories. *Biophysical Journal* 109(8):1528–1532.
46. Kolinski A, Skolnick J (1997) Determinants of secondary structure of polypeptide chains: Interplay between short range and burial interactions. *Journal of Chemical Physics* 107(3):953–964.
47. Ding F, Jha RK, Dokholyan N V. (2005) Scaling behavior and structure of denatured proteins. *Structure* 13(7):1047–1054.
48. Pasi M, Zakrzewska K, Maddocks JH, Lavery R (2017) Analyzing DNA curvature and its impact on the ionic environment: Application to molecular dynamics simulations of minicircles. *Nucleic Acids Research* 45(7):4269–4277.
49. Blanchet C, Pasi M, Zakrzewska K, Lavery R (2011) CURVES+ web server for analyzing and visualizing the helical, backbone and groove parameters of nucleic acid structures. *Nucleic Acids Research* 39(2). doi:10.1093/nar/gkr316.
50. Arya G, Schlick T (2009) A tale of tails: how histone tails mediate chromatin compaction in different salt and linker histone environments. *Journal of Physical Chemistry A* 113(16):4045–4059.
51. Beard D a, Schlick T (2001) Modeling salt-mediated electrostatics of macromolecules: the discrete surface charge optimization algorithm and its application to the nucleosome. *Biopolymers* 58(1):106–115.
52. Collepardo-Guevara R, Schlick T (2011) The effect of linker histones nucleosome binding affinity on chromatin unfolding mechanisms. *Biophysical Journal* 101(7):1670–1680.
53. Zhang Q, Beard DA, Schlick T (2003) Constructing Irregular Surfaces to Enclose Macromolecular Complexes for Mesoscale Modeling Using the Discrete Surface Charge Optimization (DiSCO) Algorithm. *Journal of Computational Chemistry* 24(16):2063–2074.
54. Arya G, Schlick T (2006) Role of histone tails in chromatin folding revealed by a mesoscopic oligonucleosome model. *Proceedings of the National Academy of Sciences of the United States of America* 103(44):16236–16241.
55. Stigter D (1977) Interactions of highly charged colloidal cylinders with applications to double-stranded DNA. *Biopolymers* 16(7):1435–1448.
56. Allison S, Austin R, Hogan M (1989) Bending and twisting dynamics of short linear DNAs. Analysis of the triplet anisotropy decay of 209 base pair fragment by Brownian simulation. *Journal of Chemical Physics* 90(7):3843–3854.
57. Allison SA (1986) Brownian Dynamics Simulation of Wormlike Chains. Fluorescence Depolarization and Depolarized Light Scattering. *Macromolecules* 19(1):118–124.
58. Jian H, Vologodskii A V., Schlick T (1997) A combined wormlike-chain and bead model for dynamic simulations of long linear DNA. *Journal of Computational Physics* 136(1):168–179.
59. Jian H, Schlick T, Vologodskii A (1998) Internal motion of supercoiled DNA: Brownian dynamics simulations of site juxtaposition. *Journal of Molecular Biology* 284(2):287–296.
60. Ilja Siepmann J, Frenkel D (1992) Conflgurational bias monte carlo: A new sampling scheme for flexible chains. *Molecular Physics* 75(1):59–70.
61. Rosenbluth MN, Rosenbluth AW (1955) Monte carlo calculation of the average extension of molecular chains.

The Journal of Chemical Physics 23(2):356–359.
62. Perišić O, Collepardo-Guevara R, Schlick T (2010) Modeling studies of chromatin fiber structure as a function of DNA linker length. *Journal of Molecular Biology* 403(5):777–802.
63. Collepardo-Guevara R, Schlick T (2012) Crucial role of dynamic linker histone binding and divalent ions for DNA accessibility and gene regulation revealed by mesoscale modeling of oligonucleosomes. *Nucleic Acids Research* 40(18):8803–8817.
64. Brown DT, Izard T, Misteli T (2006) Mapping the interaction surface of linker histone H1(0) with the nucleosome of native chromatin in vivo. *Nature Structural & Molecular Biology* 13(3):250–255.
65. Bystricky K, Heun P, Gehlen L, Langowski J, Gasser SM (2004) Long-range compaction and flexibility of interphase chromatin in budding yeast analyzed by high-resolution imaging techniques. *Proceedings of the National Academy of Sciences of the United States of America* 101(47):16495–16500.